Received 23 June 2022; revised 1 August 2022; accepted 2 August 2022. Date of publication 11 August 2022; date of current version 25 August 2022.

Digital Object Identifier 10.1109/OJAP.2022.3198290

Using an Equivalent-Circuit Model to Design Ultra-Wide Band-Stop Frequency-Selective Surface for 5G mm-Wave Applications

DEISY F. MAMEDES (Member, IEEE), AND JENS BORNEMANN (Life Fellow, IEEE)

Department of Electrical and Computer Engineering, University of Victoria, Victoria, BC V8W 2Y2, Canada

CORRESPONDING AUTHOR: J. BORNEMANN (e-mail: j.bornemann@ieee.org)

This work was supported by the Natural Sciences and Engineering Research Council (NSERC) of Canada.

ABSTRACT In this work we propose a system of two frequency-selective surfaces (FSSs) with an ultra-wide band-stop response for 5G millimeter-wave applications. The analyses are based on the equivalent circuit method, which predicts the transmission characteristics for a plane wave with normal and oblique incidence, and the scattering matrix technique, which provides the result of the cascaded structure. The geometries used in the single-layer FSSs are simple to design, and a series of basic equations are described in order to calculate the inductance and capacitance of conducting strips. FSSs prototypes were fabricated and measured in an anechoic chamber. The first FSS is shaped with the four-arms star geometry, which has a resonant frequency at 27.92 GHz for both measured and simulated results. The second FSS is based on the quasi-square geometry, whose resonant frequency for the experimental and numerical results are 35.68 GHz and 35.76 GHz, respectively, for the transverse electric polarization. These two single-layer FSSs present theoretical resonant frequency at 28 GHz (FSS #1) and 35.8 GHz (FSS #2). Cascading of the two FSSs was realized by using an air gap whose effect was analyzed. A gap space in the order of about $\lambda/4$ matched with the predicted resonant frequency of the individual structures. Numerical and measured results show excellent agreement with a maximum error of 1.03%. All measured results closely follow those of simulated ones, thus validating the design approach and applications.

INDEX TERMS Equivalent circuit, frequency-selective surfaces, cascaded FSSs, ultra-wideband.

I. INTRODUCTION

FREQUENCY-SELECTIVE surfaces (FSSs) have been intensely studied in the last five decades for their wide applications from microwave to terahertz frequencies [1], [2], [3], [4]. FSSs have been applied in antenna radomes [5], [6], reconfigurable antennas [7], [8], polarization converters [9], [10], intelligent walls [11], [12], radar cross-section reduction [13], [14] and flat lenses [15], [16]. Essentially, FSSs are two-dimensional arrays of periodic structures, formed by patch or aperture elements etched on a dielectric substrate, providing filtering properties of the incident electromagnetic waves [1], [17]. For 5G applications, FSSs are used to improve signal transmission, e.g., by blocking an unwanted signal, or as a reflector to improve an antenna's performance. Other potential usage include dual-band operation, the provision of electromagnetic shielding, and potential near-field applications [18]. The FSS frequency response depends on the thickness and electromagnetic characteristics of the dielectric material, periodicity and geometry of the elements, and the polarization and angle of the incident wave, as shown, as an example, in Fig. 1.

Single-layer FSS structures behave as a first-order filter with narrow band-pass or band-stop response [19]. Although this type of FSS is easy to design and synthesize, it is very difficult to improve the bandwidth. With the new generation, wideband antennas have experienced a boost to meet their requirements, and the need for FSSs to operate over a wide range of frequencies to enhance the performance of wide-band antenna systems has increased [20], [21]. In order to address this limitation, researchers have proposed the design

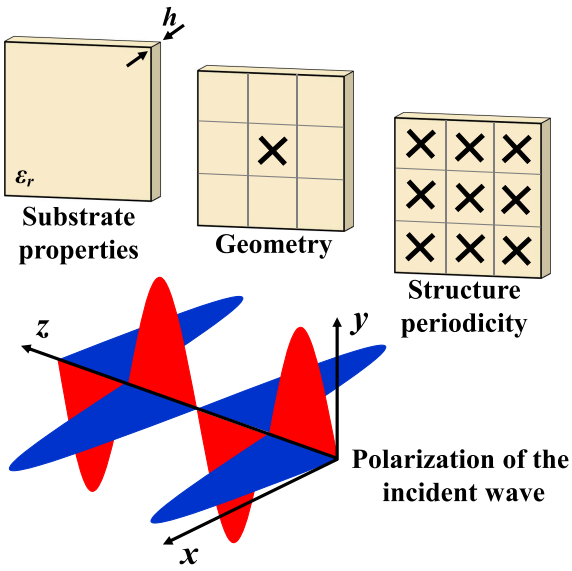

FIGURE 1. Parameters that affect the FSS frequency response.

of FSS with multiple layers as an alternative to achieve higher order filter performance, which provides a multiband or broadband response [22]. The single-layer structures are cascaded with dielectric slabs, with or without air gap in between, spacing them at approximately one quarter of the guided wavelength [23], [24].

A second-order band-pass FSS with wide out-of-band rejection from 1 to 40 GHz is presented in [25] where an equivalent circuit model was established. The FSS provides a band-pass response operating at 10 GHz with 12% fractional bandwidth.

A new technique with a low-profile FSS with third-order band-pass responses was proposed in [22]. The structure is composed by cascading three metal layers, separated by two thin dielectric substrates. The prototype FSS shows good results, operating at C band frequencies.

A three-layer FSS is described in [26] with an ultra-wideband band-stop response. The structure is formed by cascaded layers of rectangular patches and rectangular patches with notches printed on dielectric substrates. The results show that the prototype covers the band from 4 to 14 GHz for vertical polarization and from 5 to 15 GHz for horizontal polarization.

The equivalent circuit model (ECM) is a method that provides characteristics of transmission from the structure to a plane wave incidence and requires less computing effort compared with field solvers. Here, capacitive and inductive components are modeled from segments of strips placed in a periodic array [27], [28]. Therefore, this paper proposes a double-layer FSS with ultra-wideband rejection response. The proposed FSS combines two single-layer FSSs with different geometry with interesting characteristics such as simple design and miniaturization, and it is analyzed and designed through ECM by simply adapting Marcuvitz's equations [29] for conductive strips. The cascaded structure covers the K (18 GHz to 26.5 GHz) and Ka band (26.5 GHz to 40 GHz), with a bandwidth of approximately 24.4 GHz, operating from 18.3 GHz to 42.7 GHz in simulated results. The proposed structure has transmission zeroes at 28 GHz and 36 GHz applicable for 5G technology, which is designed to reflect signals in the range of frequency from K to Ka band. It is important to mention that distinguished bands have been allocated in each region [30], and the proposed FSS is suitable in different bands and frequencies, while offering high bandwidth. The resonant frequencies and bandwidth can be adjusted by optimizing the dimensions of the proposed FSS. A prototype was fabricated and measured, and experimental results show excellent agreement with simulations.

II. EQUIVALENT CIRCUIT MODEL

A. REVIEW

Studies of fundamental equations have been published to determine the transmission and reflection coefficients of FSSs. In 1946, MacFarlane [31] demonstrated that the scattering problem of a parallel wire grid could be solved using a transmission line model (TLM). Marcuvitz [29] showed that FSS structures can be represented by an equivalent circuit (EC), considering the transverse electric, TE, and transverse magnetic, TM, incidence on conductive strips. Chen [32] and Ulrich *et al.* [33] improved the EC to consider resonant effects of the structures. Reference [34] presented a refined version of Chen's and Ulrich's formulas. Furthermore, the formula was extended to approximate solutions for cascading screens and dielectric slabs. In the 80s, derivate formulas have been reported for more complex FSS geometries and achieved accurate results, as demonstrated by Langley [35], [36], [37], [38].

A complementary FSS (CFSS) is proposed in [28], which is defined as patch and slot elements of same size and shape arranged on either side of a substrate, based on Babinet's principle. An ECM compounded with TLM was employed to analyze the CFSS response. The method presented a good accuracy of the scattering parameters, for normal and oblique incidence, allowing to estimate the frequency response with less error. The efficacy of the ECM results was verified with commercial software.

A wideband FSS operating in Ka-band is presented in [39]. A multi-layer structure was adopted to enhance the passband, and the coupling between the capacitive and inductive surfaces was employed to miniaturize the structure to 0.26 λ. The ECM was applied to give a better understanding of the structure's behavior and its frequency response.

The ECM is introduced in [40] to explain the effect of a convoluted geometry structure on the frequency response of an FSS. Measured and simulated results showed that the FSS proposed has a good stability under different polarizations and incidence angles.

An accurate analytical procedure is described in [41] for wideband nonmagnetic absorbers operating at lower

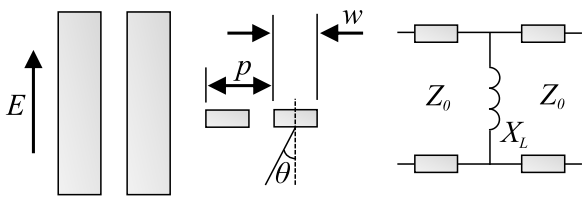

FIGURE 2. Incidence parameters considering strip arrangement and angle, and equivalent circuit for TE polarization.

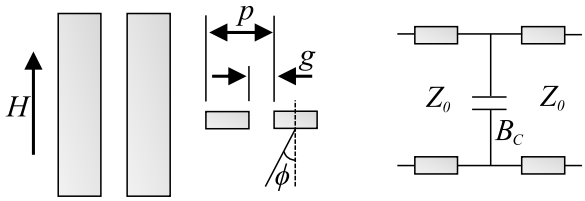

FIGURE 3. Incidence parameters considering strip arrangement and angle, and equivalent circuit for TM polarization.

microwave frequencies. An ECM was designed, based on the simulated data and synthetic asymptotes for single and double-layer FSSs. Several designs of broadband absorbers were demonstrated by employing the ECM and genetic algorithm-based optimization. Those results were compared to full-wave methods, showing more than 95% accuracy.

B. METHOD

FSS design and analysis can be done by modelling its EC, which uses less computational effort compared to full-wave methods. Also, it provides a better electromagnetic understanding of the structure considered. Marcuvitz [29] demonstrated that an FSS is modelled as an infinite array of parallel conducting strips, and it can be represented by capacitive and inductive elements. Fig. 2 shows the EC for a TE incidence when the conducting strips are parallel to the electric field; in this configuration, the FSS is represented by an inductance. In the other case, Fig. 3, the conducting strips are parallel to the magnetic field, and the FSS is associated with a capacitance. The strip parameters are width w, periodicity p, spaced distance g, and incidence angles of θ and ϕ for incident plane waves, TE and TM, respectively.

To determine the EC, the general formulas for the inductive reactance, X_L, and capacitive susceptibility, B_C, are [36]:

$$\frac{X_L}{Z_0} = F(p, w, \lambda, \theta) = \frac{p\cos\theta}{\lambda}\left\{\ln\left[\csc\left(\frac{\pi w}{2p}\right)\right] + G(p, w, \lambda, \theta)\right\} \quad (1)$$

$$\frac{B_C}{Y_0} = 4F(p, g, \lambda, \phi) = \frac{4p\cos\theta}{\lambda}\left\{\ln\left[\csc\left(\frac{\pi g}{2p}\right)\right] + G(p, g, \lambda, \phi)\right\} \quad (2)$$

where λ is the wavelength, and G is a correction factor that allows incidence of the plane waves at arbitrary angles by varying θ and ϕ.

$$G(p, w, \lambda, \theta) = \frac{0.5(1-A^2)^2\left[\left(1-\frac{A^2}{4}\right)(B_+ + B_-) + 4A^2B_+B_-\right]}{\left(1-\frac{A^2}{4}\right) + A^2\left(1+\frac{A^2}{2}-\frac{A^4}{8}\right)(B_+ + B_-) + 2A^6B_+B_-} \quad (3)$$

Note that when calculating the capacitive susceptibility, the function G can be solved by replacing ϕ with θ and w with g.

$$A = \sin\left(\frac{\pi w}{2p}\right) \quad (4)$$

$$B_\pm = \left[1 \pm \frac{2p\sin\theta}{\lambda} - \left(\frac{p\cos\theta}{\lambda}\right)^2\right]^{-\frac{1}{2}} - 1 \quad (5)$$

Equations (1) and (2) have limitations and must meet the following conditions $w/p \ll 1$, $p/\lambda \ll 1$, and $p(1+\sin\theta)/\lambda < 1$. They are not suitable for modelling of cross polarization [35].

The elements are printed on a dielectric substrate which modifies the capacitance of the FSS as a function of the dielectric permittivity ϵ_r, and thickness of the substrate h. For thin substrates involving higher-order Floquet modes, a closed formula based on Green's functions cannot be pursued. Reference [42] presents an interpolating formula that fits the variation of the effective permittivity $\epsilon_{r_{eff}}$, according to the dielectric thickness by manipulating an exponential function. The effective electrical permittivity is given by:

$$\epsilon_{r_{eff}} = \epsilon_r + (\epsilon_r - 1)\left[\frac{-1}{e^{M\frac{10h}{p}}}\right] \quad (6)$$

where M is an exponential factor, which takes into account the slope of the curve that depends on the unit cell filling.

III. SINGLE-LAYER FSS ANALYSIS AND DESIGN

This section presents the design of two simple geometries with simplified formulation. The equations for their equivalent circuit are straightforwardly implemented in MATLAB.

A. FOUR-ARMS STAR GEOMETRY

The first FSS designed (FSS #1) is based on the four-arms star geometry, which has demonstrated very interesting characteristics such as miniaturization and switching, applicable to reconfigurable antennas [7], [43] and FSS [44], and as polarization converter [45]. Initially, the unit cell dimension is defined as p, and then a rectangular patch is designed as a, where the arms are shaped. From the edges, lines cross the rectangular patch with b and the four-arms star geometry is achieved. A small square patch of width s is etched at

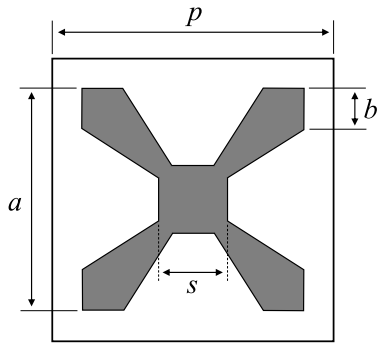

FIGURE 4. Geometry and parameters of FSS #1.

the center to connect all the arms. Finally, the outside of the four arms are detached from the metallic surface and the four-arms star is completed (Fig. 4).

The normalized inductive reactance X_f and the normalized capacitive susceptance B_f of the structure based on the four-arms star geometry are defined as

$$\frac{X_{L_f}}{Z_0} = 1.5\frac{a}{p}F(p, b, \lambda, \theta) \tag{7}$$

$$\frac{B_{C_{g_f}}}{Y_0} = \frac{4b}{1.5p}F(p, g_{f_1}, \lambda, \phi) \tag{8}$$

$$\frac{B_{C_{a_{1_f}}}}{Y_0} = \frac{4(p-b)}{1.5p}F(p, g_{f_2}, \lambda, \phi) \tag{9}$$

$$\frac{B_{C_{a_{2_f}}}}{Y_0} = 4\frac{(p-s)}{p}F(p, g_{f_3}, \lambda, \phi) \tag{10}$$

The presence of dielectric support is taken into account in the ECM by including its dielectric effective permittivity value in the capacitive elements of the circuit.

$$\frac{B_{C_{1_f}}}{Y_0} = \left(B_{C_{a_{1_f}}} + B_{C_{g_f}}\right)\epsilon_{r_{eff_f}} \tag{11}$$

$$\frac{B_{C_{2_f}}}{Y_0} = 0.25\left(B_{C_{a_{2_f}}} + B_{C_{g_f}}\right)\epsilon_{r_{eff_f}} \tag{12}$$

The admittance of the EC of the four-arms star is given by

$$Y_f = \frac{1}{X_{L_f} - \frac{1}{B_{C_{1_f}}}} - \frac{1}{\frac{1}{B_{C_{2_f}}}} \tag{13}$$

The transmission coefficient is found by

$$\sigma_f = \frac{1}{1 + 0.25Y_s^2} \tag{14}$$

The reflection coefficient is given by

$$\Gamma_f = \sqrt{1 - \sigma_s^2} \tag{15}$$

Reference [45] presents the equations to determine the resonant frequency for the FSS using the four-arms star geometry from initial dimensions. Based on this design procedure the FSS was designed to operate at 28 GHz and

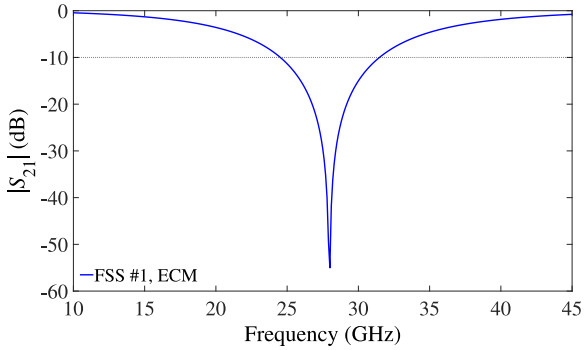

FIGURE 5. Theoretical result for FSS #1.

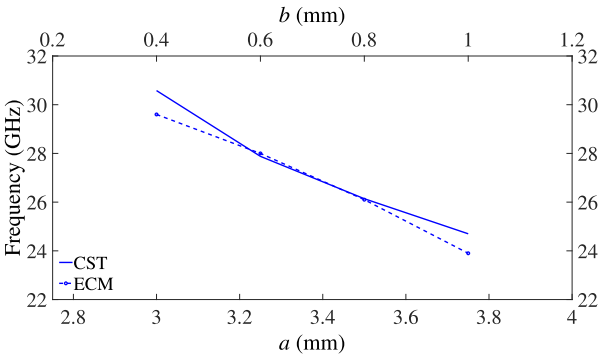

FIGURE 6. Influence of FSS #1 frequency response, with dimensions $p = 4.1$ mm and $s = 1.0$ mm, and substrate permittivity $\epsilon_r = 2.94$ and 0.508 mm thickness.

adapted to the ECM. The dimension of the structure are $p = 4.1$ mm, $a = 3.25$ mm, $s = 1.0$ mm and $b = 0.6$ mm, and considering a dielectric substrate with $\epsilon_r = 2.94$ and thickness of 0.508 mm. The value of M is 2.4 for the four-arms star geometry. Fig. 5 illustrates the theoretical result, with resonant frequencies at 28 GHz (−55.01 dB) and bandwidth of 7 GHz (from 24.5 GHz to 31.5 GHz).

A comparison between the resonant frequency of FSS #1 in terms of the arms' size obtained by ECM and CST Microwave Studio is illustrated in Fig. 6. Change in the arms' size changes the gap between copper and the unit cell, which increase the inductance and capacitance, leading to lower resonant frequencies. The dimensions of the unit cell and square in the center are fixed with $p = 4.1$ mm and $s = 1.0$ mm. The increase in the parameters a (from 3 to 3.75 mm) and b (from 0.4 to 0.6 mm) leads to the reduction of the resonant frequency.

The proposed FSS is analyzed by the ECM and CST, considering different dielectric permittivities of commercial substrates. Fig. 7 shows the resonant frequencies versus substrate thickness. All curves follow the same profile, proving that the model can be used for any substrate. The increase in the thickness translates to the reduction in resonant frequency.

B. QUASI-SQUARE GEOMETRY

The second geometry proposed is shown in Fig. 8 (FSS #2). To design it, initially a square patch p is dimensioned. Slot

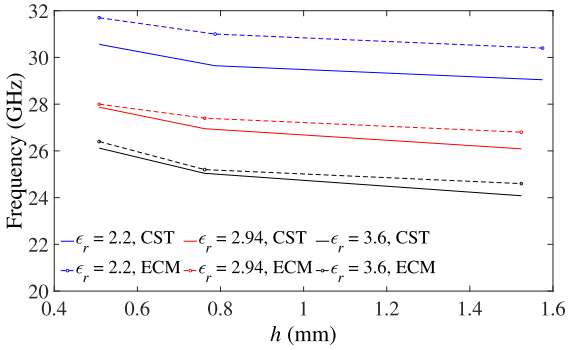

FIGURE 7. Comparison of resonant frequencies as a function of dielectric permittivity while variating the substrate thickness of FSS #1.

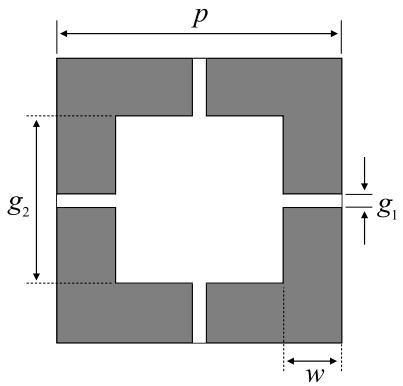

FIGURE 8. Geometry and parameters of FSS #2.

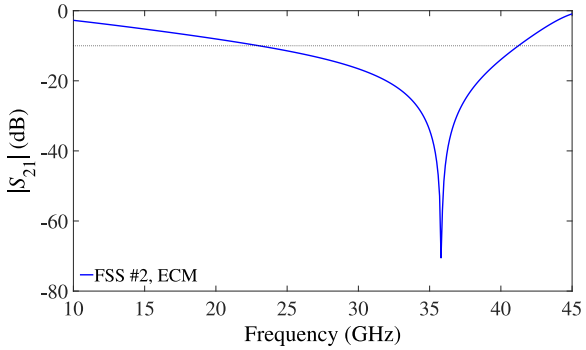

FIGURE 9. Theoretical result for FSS #2.

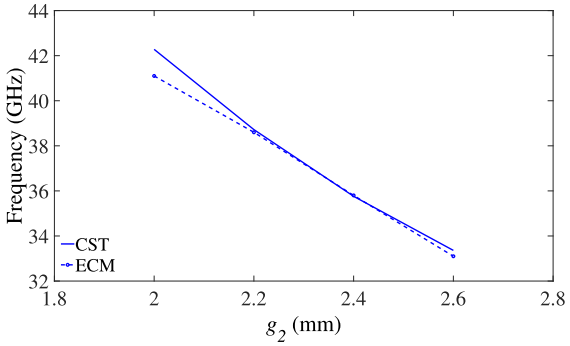

FIGURE 10. Influence of FSS #2 frequency response, with dimensions $p = 4.1$ mm and $g_1 = 0.2$ mm, and substrate permittivity $\epsilon_r = 2.94$ and 0.508 mm thickness.

sections are inserted, crossing it in the middle, both vertically and horizontally, of width g_1. In this part, the FSS behaves as a capacitor with a wideband response. The final step to achieve the geometry is to add a square slot of size g_2, in the center of the patch, and the metallic surface has a width of w. Depending on the size of this square, the FSS starts increasing its inductance and hence, its resonant frequency and bandwidth decrease.

The inductive reactance X_s and the capacitive susceptance B_s normalized to the intrinsic impedance of free space ($Z_0 = 1/Y_0$), of the quasi-square FSS are

$$\frac{X_{L_s}}{Z_0} = 0.5\frac{(p-w)}{p}F(p,w,\lambda,\theta) \tag{16}$$

$$\frac{B_{C_{sg_1}}}{Y_0} = 4\frac{w}{p}F(p,g_1,\lambda,\phi) \tag{17}$$

$$\frac{B_{C_{sg_2}}}{Y_0} = 4\frac{(p-w)}{p}F(p,g_2,\lambda,\phi) \tag{18}$$

$$\frac{B_{C_{1_s}}}{Y_0} = 0.5B_{C_{sg_1}}\epsilon_{r_{effs}} \tag{19}$$

$$\frac{B_{C_{2_s}}}{Y_0} = 0.25\left(B_{C_{sg_2}} + B_{C_{sg_1}}\right)\epsilon_{r_{effs}} \tag{20}$$

The admittance is calculated as

$$Y_s = \frac{1}{X_{L_s} - \frac{1}{B_{C_{1_s}}}} - \frac{1}{\frac{1}{B_{C_{2_s}}}} \tag{21}$$

The transmission coefficient (σ_s) can be calculated from Eq. (14) by replacing the admittance Y_f with the admittance of the second FSS (Y_s). Hence, the reflection coefficient (Γ_s) for the quasi-square FSS is found from Eq. (15), by using the calculated value of σ_s.

This second FSS was designed for 35.8 GHz, and the properties of the dielectric substrate are the same used for FSS #1. The unit cell has the same size as that of FSS #1, $p = 4.1$ mm. The design is numerically optimized until the desired characteristics are achieved with dimensions $w = 0.85$ mm, $g_1 = 0.2$ mm and $g_2 = 2.4$ mm. For the geometry proposed, the value of M is 1.5. Fig. 9 shows the numerical result of the transmission coefficient, with the resonant frequency at 35.8 GHz (−70.52 dB) and −10-dB bandwidth of 18.2 GHz (from 23 GHz to 41.2 GHz).

The effect in the resonant frequency as a function of the size of g_2 as analyzed by ECM is presented in Fig. 10. The other parameters are fixed, except for w that is inversely proportional to g_2. The capacitance and inductance is proportional to an increase of g_2, thus leading to a gradual reduction of the resonant frequency.

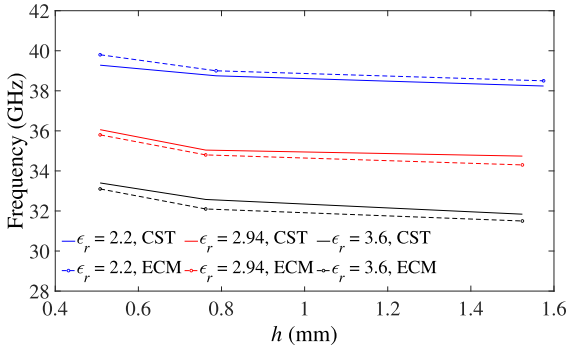

FIGURE 11. Comparison of resonant frequencies as a function of dielectric permittivity while variating the substrate thickness of FSS #2.

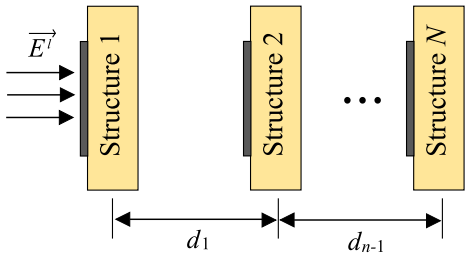

FIGURE 12. Cascading *N* FSS structures.

The applicability of ECM for FSS #2 considering different dielectric permittivities of substrates is compared to a full-wave method. The dimensions of the structure are the ones used to obtain the result in Fig. 9. Fig. 11 shows the resonant frequencies versus substrate thickness. As expected, the results prove that the model can be used for any substrate. To provide a comparison of CPU times between the two methods, for the example with $\epsilon_r = 3.6$ and $h = 0.762$ mm, the ECM was approximately 390 times faster than CST.

IV. CASCADED FSS

The cascading of FSSs is used to obtain an ultra-wide band-stop response by exploiting multiple resonances. Each single-layer structure provides a different transmission zero as shown in Section III. In order to compute the performance of N cascaded structures separated by a distance d_{n-1} (Fig. 12), the scattering matrix can be applied using single-mode interaction.

In this section, the two single-layer structures presented in the previous section are cascaded, and the 2×2 scattering matrix $[S]$ is determined as

$$\bar{\bar{S}}_n = \begin{bmatrix} \sigma_n\left(1 - \frac{\Gamma_n^2}{\sigma_n^2}\right) & \left(\frac{\Gamma_n}{\sigma_n}\right)e^{j2kl_n} \\ -\left(\frac{\Gamma_n}{\sigma_n}\right)e^{-j2kl_n} & \frac{1}{\sigma_n} \end{bmatrix} \tag{22}$$

where

$$l_n = d_1 + d_2 + \cdots + d_{n-1}, \tag{23}$$

$n = 1, 2, \ldots, N$

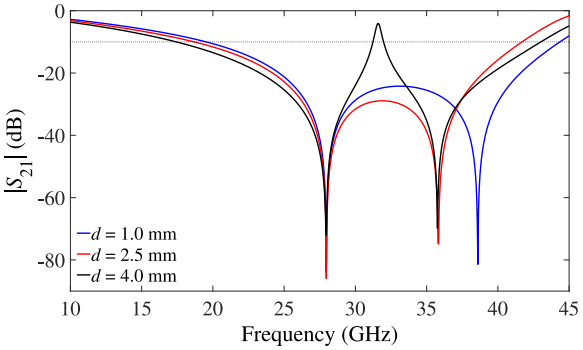

FIGURE 13. Simulated results for cascaded FSS, considering different spacing.

The matrix with C, D, E, F elements is given as

$$\begin{bmatrix} C & D \\ E & F \end{bmatrix} = \bar{\bar{S}}_n \bar{\bar{S}}_{n-1} \cdots \bar{\bar{S}}_3 \bar{\bar{S}}_2 \bar{\bar{S}}_1 \tag{24}$$

Applying the single-mode iteration, the total transmission and reflection coefficients are [28]

$$\sigma = C - \frac{DE}{F} \tag{25}$$

$$\Gamma = -\frac{E}{F} \tag{26}$$

The coupling between the two structures is determined by their spatial separation d. The influence of the coupling, considering an air gap with different spacing ($d = 1.0$ mm, 2.5 mm and 4.0 mm) is presented in Fig. 13. In the first analysis with spacing $d = 1.0$ mm, the resonant frequencies are 27.96 GHz and 38.6 GHz, with a -10-dB bandwidth of 24.82 GHz. In the second case, $d = 2.5$ mm, the resonant frequencies are 27.96 GHz and 35.84 GHz, with 23.02 GHz of bandwidth. It can be seen in the third case ($d = 4$ mm) that the numerical result is about the same as for the individual structures, presenting two stop-bands, the first resonant frequency f_{z_1} is at 27.96 GHz with 13.8 GHz of bandwidth and the second resonant frequency f_{z_2} is at 35.76 GHz with 11.04 GHz of bandwidth. This last case also presents a resonant frequency at 31.6 GHz (-4.07 dB) with a band-pass behavior. With the increase of coupling (increasing the spacing d), the anti-parallel currents are induced in the resonators, causing the destructive interference of scattering fields. The transparency window becomes stronger for $d = 4$ mm, and this behavior is known as the Electromagnetically Induced Transparency (EIT) effect, which is a physical phenomenon that eliminates the effect of a medium in an electromagnetic radiation [46], [47], [48].

These results are summarized in Table 1, showing the difference when compared to the individual FSSs.

Fig. 14 compares the theoretical results of the individual structure and cascaded one by applying ECM. These results indicate that the prediction in terms of frequency response of the cascaded FSS follows the ones from the single-layer FSSs, with larger bandwidth and multiple resonances. It can be noticed that the two transmission zeroes in the cascaded

TABLE 1. Comparison of resonant frequencies between individual and cascaded FSSs.

Structure	f_{z_1} (GHz)	Diff. (%)	f_{z_2} (GHz)	Diff. (%)
FSS #1	28	—	—	—
FSS #2	—	—	35.8	—
1st Cascade (d = 1.0 mm)	27.96	0.14	38.6	7.82
2nd Cascade (d = 2.5 mm)	27.96	0.14	35.84	0.11
3rd Cascade (d = 4.0 mm)	27.96	0.14	35.76	0.11

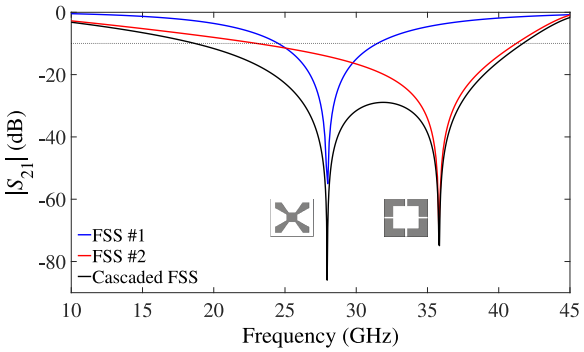

FIGURE 14. Comparison of numerical results of individual FSSs and cascaded one.

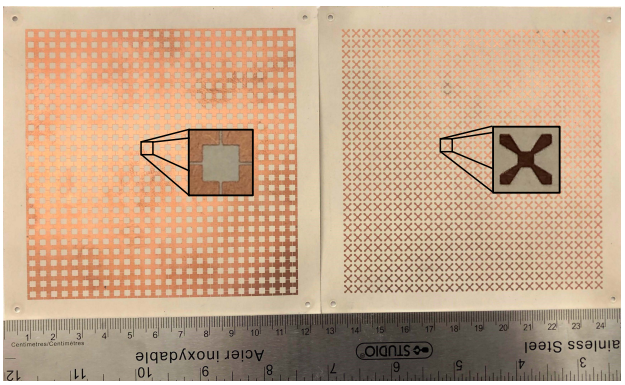

FIGURE 15. Fabricated FSSs with quasi-square (left) and four-arms star (right) geometries, and their individual cells.

FSS are created by the resonators in each layer and the ultra-wide band-stop by the EIT effect. The cascading was done considering an air gap of $d = 2.5$ mm between the two FSSs as shown in Fig. 13. The two resonant frequencies are 27.96 GHz (−85.96 dB) and 35.84 GHz (−74.91 dB) and the mutual coupling resulted in a −10-dB bandwidth of 23.02 GHz.

V. RESULTS

Two FSSs with the proposed geometries were manufactured to validate the numerical results by experiments. The prototypes were fabricated on single-layer Rogers Duroid/RT 6002 dielectric substrate with $\epsilon_r = 2.94$, thickness of 0.508 mm, and loss tangent of 0.0012, with 26 × 26 elements and overall dimensions of 10.7 cm × 10.7 cm (Fig. 15).

FIGURE 16. Measurement setup.

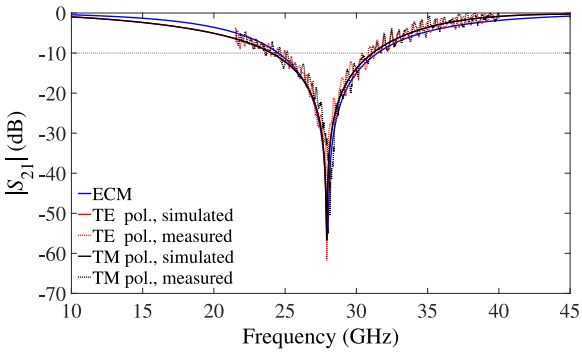

FIGURE 17. Simulated and measured results for prototype FSS #1.

Measurements were carried out in an anechoic chamber, the prototype is placed in the stand between the transmitting (T_x) and receiving (R_x) antennas (Fig. 16). Two horn antennas were used with a distance of 80 cm, the T_x one is LB-28-25-C-KF (26.5-40 GHz) and the R_x is LB-180400H-KF (18-40 GHz), connected to a Vector Network Analyzer model Anritsu 37397c, a normal wave incidence is considered to the FSS. The calibration procedure to test the manufactured structures consisted of two steps. The first one is to calibrate the cables using short-open-load-through (SOLT) terminations. Secondly, the T_x and R_x antennas are aligned, and its transmission coefficient is measured, as the reference of transmissivity. Then, the results of the FSSs under test are normalized to the reference.

Note that in both FSSs the geometries are symmetric in the x- and y-direction, i.e., the frequency response is independent of the electric field polarization, therefore the results for both polarization are similar. The measured transmission coefficients of the fabricated structures, considering single- and double-layers, under normal incidence along with the numerical characterizations obtained by ECM and CST are presented for TE and TM polarizations.

Fig. 17 presents the simulated and measured transmission coefficients for the first structure. For the TE polarization, the measured resonant frequency is 27.92 GHz compared to simulated ones of 27.92 GHz from CST and 28 GHz for ECM, thus showing excellent agreement with a maximum

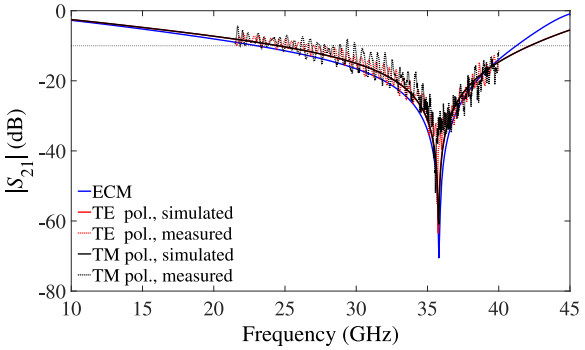

FIGURE 18. Simulated and measured results for prototype FSS #2.

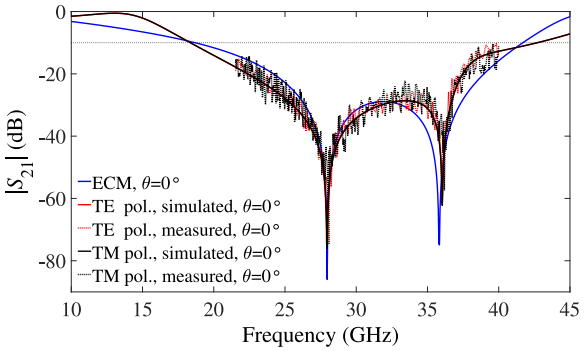

FIGURE 19. Simulated and measured results for cascaded FSS at normal incidence.

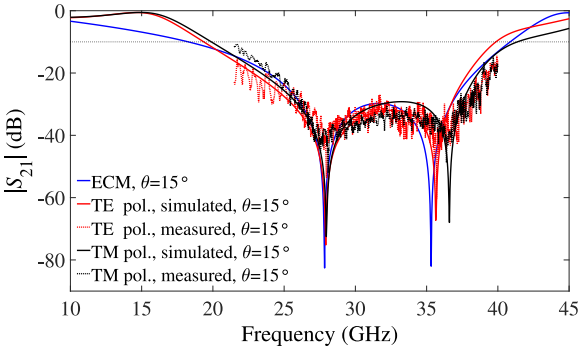

FIGURE 20. Simulated and measured results for cascaded FSS off-normal incidence.

difference of only 0.28%. The −10-dB bandwidth obtained for the measured and simulated results are 6.88 GHz (experimental), 7.08 GHz (CST) and 7 GHz (ECM). A CPU time comparison reveals that using the theoretical equations presented in Section III is at least 280 times faster than CST. In the TM polarization, the results are very similar with resonant frequencies at 27.92 GHz (CST) and 28.16 GHz (measured), with maximum difference of 0.57%, and bandwidth of 7.08 GHz and 7.02 GHz for numerical and experimental results.

The FSS #2 was designed for 35.8 GHz. Fig. 18 shows the comparison between numerical (CST and ECM) and experimental results, with resonances at 35.76 GHz, 35.8 GHz and 35.68 GHz, respectively – a maximum difference of 0.33%, for the TE polarization. The bandwidth in this polarization in the simulation is 17.68 GHz (CST) and 18.2 GHz (ECM). The measurement goes up to 40 GHz (antenna's maximum frequency), thus we were unable to measure the entire bandwidth. However, it is obvious that the measured result shows the same behavior as the simulation. A comparison of CPU times between the two methods shows that our ECM was 250 times faster than CST. In the TM polarization, the resonant frequency is 35.8 GHz (CST) and 35.56 GHz (measured), with a maximum difference of 0.67%, and −10-dB bandwidth of 17.64 GHz.

Fig. 19 shows the measured transmission coefficient along with numerical results for the cascaded FSS. The air gap between the structures is 2.5 mm based on Fig. 13, provided by using Teflon spacers, nuts and screws to complete the cascade. The measured transmission zeros in the TE polarization are 28.08 GHz (−74,73 dB) and 36 GHz (−57.19 dB), and show excellent agreement with those obtained by CST ($f_{z1} = 27.92$ GHz and $f_{z2} = 36.04$ GHz) and our ECM ($f_{z1} = 27.96$ GHz and $f_{z2} = 35.84$ GHz), with a maximum difference of 0.28% and 0.67%, respectively. From numerical results, the cascaded FSS has a bandwidth of 24.38 GHz (CST) and 23.02 GHz (ECM), going from 18.34 to 42.72 GHz and 18.68 to 41.70 GHz, respectively. Due to limitations in the frequency range of the horn antennas used, the measured results are shown from 21.5 GHz to just 40 GHz, although it can be observed that the experimental curve closely follows the numerical one. The theoretical method also showed to be faster than CST for the cascaded FSS in order of 345 times. The characterization of the TM polarization was also performed, and due to the symmetry of the structure, the results obtained are very similar to the TE polarization. The two occurring transmission zeros are 28.02 GHz and 36.17 GHz for the measured results, and the numerical ones are 27.96 GHz and 36.04 GHz (CST), with a maximum difference of 0.14% and 1.03%, respectively. The numerical bandwidth is 24.36 GHz with a band-stop range from 18.34 GHz to 42.70 GHz.

The transmission coefficients of simulated and measured results for TE and TM polarization off-normal incidence with $\theta = 15°$ is shown in Fig. 20. The results obtained numerically show that the proposed FSS presents a wide bandwidth of approximately 22.6 GHz (ECM), and 20.5 GHz (CST—TE pol.) and 21.48 GHz (CST—TM pol.).

A detailed comparison between the proposed FSS and other previously reported ones, including their type of configuration, 10-dB fractional bandwidth, number of transmission zeros and unit cell dimensions, is shown in Table 2. It can be seen that the resonances depend mainly on the number of layers as it is for the bandwidth response, besides the complexity of the structure's geometry. The proposed FSS demonstrates to have wider bandwidth when compared to others, only using two layers with simple geometries.

TABLE 2. Comparison of proposed FSS with other reported ones.

Ref.	Configuration	10-dB bandwidth (%)	Resonances	Unit cell size
[49]	2-D single layer	47.6	1	$0.25\lambda \times 0.25\lambda$
[50]	2-D single layer	50.0	1	$0.37\lambda \times 0.74\lambda$
[51]	3-D cascaded annular ring	53.8	2	$0.48\lambda \times 0.48\lambda$
[52]	2-D double layer	54.5	2	$0.34\lambda \times 0.34\lambda$
[53]	2-D double layer	54.5	3	$0.20\lambda \times 0.20\lambda$
[54]	2-D three layers	68.4	3	$0.23\lambda \times 0.23\lambda$
This work	2-D double layer	79.8	2	$0.41\lambda \times 0.41\lambda$

VI. CONCLUSION

An ultra-wide band-stop double-layer FSS is proposed in this paper, operating at K (18 GHz to 26.5 GHz) and Ka band (26.5 GHz to 40 GHz), with resonant frequencies compatible to 5G mm-wave applications. It is demonstrated that combining FSSs with simple geometries can obtain a wide-band response. A simple modeling of the resonant frequency behavior of the FSSs is proposed and validated, both through computer simulations and measurement of prototypes. The procedure used for computing the inductance and capacitance of the FSSs is described by modeling segments of strips by basic equations. The analyzes of the single-layer structures and cascaded one are also performed by full-wave simulations using CST. The air gap spacing parameter is analyzed, the gap with the distance of about $\lambda/4$, considering the center frequency at 30 GHz, shows to have a better match to the resonant frequencies of the individual FSSs, with less discrepancy as shown in Table 1. The air gap between the structures also allows to control the bandwidth. Numerical and measured results show excellent agreement, with a maximum difference of 1.03%. Although it was not possible to measure the entire bandwidth of FSS #2 and the cascaded structure due to limitation in the frequency range of the horn antennas used, it can be seen that the experimental curves in both cases closely follow the ones obtained from the simulations. In all investigated cases, the theoretical method was several hundred times faster than CST, just establishing itself as an excellent option for a first and fast analysis of single-layer and cascaded FSSs.

REFERENCES

[1] B. A. Munk, "Element types: A comparison," in *Frequency Selective Surfaces: Theory and Design*. Hoboken, NJ, USA: Wiley, 2000, pp. 50–51.

[2] B. Munk, R. Kouyoumjian, and L. Peters, "Reflection properties of periodic surfaces of loaded dipoles," *IEEE Trans. Antennas Propag.*, vol. 19, no. 5, pp. 612–617, Sep. 1971.

[3] B. Li, Y.-S. Zeng, B.-J. Chen, and C. H. Chan, "Terahertz frequency-selective surface with polarization selection and conversion characteristics," *IEEE Trans. THz Sci. Technol.*, vol. 9, no. 5, pp. 510–519, Sep. 2019.

[4] D. Montofre, A. Khudchenko, F. P. Mena, R. Hesper, and A. M. Baryshev, "Single-layer dichroic filters for multifrequency receivers at THz frequencies," *IEEE Trans. THz Sci. Technol.*, vol. 10, no. 6, pp. 690–697, Nov. 2020.

[5] A. A. Omar and Z. Shen, "Thin 3-D bandpass frequency-selective structure based on folded substrate for conformal radome applications," *IEEE Trans. Antennas Propag.*, vol. 67, no. 1, pp. 282–290, Jan. 2019.

[6] B. Sangeetha, G. Gulati, R. U. Nair, and S. Narayan, "Design of airborne radome using Swastika-shaped metamaterial-element based FSS," in *Proc. IEEE Annu. India Conf. (INDICON)*, 2016, pp. 1–5.

[7] D. F. Mamedes, A. G. Neto, and J. Bornemann, "Reconfigurable corner reflector using PIN-diode-switched frequency selective surfaces," in *Proc. IEEE Int. Symp. Antennas Propag.*, 2020, pp. 127–128.

[8] S. M. Mahmood and T. A. Denidni, "Pattern-reconfigurable antenna using a switchable frequency selective surface with improved bandwidth," *IEEE Antennas Wireless Propag. Lett.*, vol. 15, pp. 1148–1151, 2016.

[9] C. Yang, P. Liu, and X. Zhu, "Circularly polarized microstrip patch antenna array based on FSS polarization converter," in *Proc. Int. Symp. Antennas Propag. (ISAP)*, 2019, pp. 1–3.

[10] F. Costa, S. Genovesi, A. Monorchio, S. Zhang, Y. Cui, and J. Liu, "Broadband linear to circular reflection polarization converter," in *Proc. IEEE Int. Symp. Antennas Propag.*, 2019, pp. 1823–1824.

[11] S. Habib, G. I. Kiani, and M. F. U. Butt, "Interference mitigation and WLAN efficiency in modern buildings using energy saving techniques and FSS," in *Proc. IEEE Int. Symp. Antennas Propag.*, 2016, pp. 965–966.

[12] M. Gustafsson, A. Karlsson, A. Rebelo, and B. Widenberg, "Design of frequency selective windows for improved indoor outdoor communication," *IEEE Trans. Antennas Propag.*, vol. 54, no. 6, pp. 1897–1900, Jun. 2006.

[13] M. Pazokian, N. Komjani, and M. Karimipour, "Broadband RCS reduction of Microstrip antenna using coding frequency selective surface," *IEEE Antennas Wireless Propag. Lett.*, vol. 17, no. 8, pp. 1382–1385, Aug. 2018.

[14] H. B. Baskey and M. J. Akhtar, "Design of flexible hybrid nanocomposite structure based on frequency selective surface for wideband radar cross section reduction," *IEEE Trans. Microw. Theory Techn.*, vol. 65, no. 6, pp. 2019–2029, Jun. 2017.

[15] Y. Suo, H. Wang, and W. Li, "C-band multi-beam planar lens antenna based on frequency selective surface," in *Proc. IEEE Int. Symp. Antennas Propag.*, 2019, pp. 727–728.

[16] S. Pandey, R. K. Arya, and R. Mittra, "Flat lens design using space-qualifiable multilayer frequency selective surfaces," in *Proc. IEEE Int. Symp. Antennas Propag. (APSURSI)*, 2016, pp. 1643–1644.

[17] R. S. Anwar, L. Mao, and H. Ning, "Frequency selective surfaces: A review," *Appl. Sci.*, vol. 8, no. 9, p. 1689, 2018.

[18] Y. Li, P. Ren, and Z. Xiang, "A dual-passband frequency selective surface for 5G communication," *IEEE Antennas Wireless Propag. Lett.*, vol. 18, no. 12, pp. 2597–2601, Dec. 2019.

[19] Y. Xu and S. Zhang, "An ultra wideband FSS operating at Ka band," in *Proc. IEEE Int. Conf. Comput. Electromagn. (ICCEM)*, 2019, pp. 1–3.

[20] M. Simruni and S. Jam, "Design of high gain, wideband microstrip resonant cavity antenna using FSS superstrate with equivalent circuit model," *AEU-Int. J. Electron. Commun.*, vol. 112, pp. 1–12, Dec. 2019.

[21] N. Kushwaha and R. Kumar, "Design of a wideband high gain antenna using FSS for circularly polarized applications," *AEU-Int. J. Electron. Commun.*, vol. 70, no. 9, pp. 1156–1163, 2016.

[22] N. Behdad, M. Al-Joumayly, and M. Salehi, "A low-profile third-order bandpass frequency selective surface," *IEEE Trans. Antennas Propag.*, vol. 57, no. 2, pp. 460–466, Feb. 2009.

[23] N. Liu, X. Sheng, C. Zhang, and D. Guo, "Design of frequency selective surface structure with high angular stability for radome application," *IEEE Antennas Wireless Propag. Lett.*, vol. 17, no. 1, pp. 138–141, Jan. 2018.

[24] A. Chatterjee and S. K. Parui, "A multi-layered band-pass frequency selective surface designed for ku band applications," in *Proc. IEEE Appl. Electromagn. Conf. (AEMC)*, 2013, pp. 1–2.

[25] N. Liu, X. Sheng, C. Zhang, and D. Guo, "Design and synthesis of band-pass frequency selective surface with wideband rejection and fast roll-off characteristics for radome applications," *IEEE Trans. Antennas Propag.*, vol. 68, no. 4, pp. 2975–2983, Apr. 2020.

[26] F. C. G. D. S. Segundo, A. L. P. D. S. Campos, and A. G. Neto, "A design proposal for ultrawide band frequency selective surface," *J. Microw. Optoelectron. Electromagn. Appl.*, vol. 12, pp. 398–409, Dec. 2013.

[27] A. R. Varkani, Z. H. Firouzeh, and A. Z. Nezhad, "Equivalent circuit model for array of circular loop FSS structures at oblique angles of incidence," *IET Microw. Antennas Propag.*, vol. 12, no. 5, pp. 749–755, 2018.
[28] V. Krushna Kanth and S. Raghavan, "Equivalent circuit analysis of complementary FSS for selective EM shielding," in *Proc. 15th Int. Conf. ElectroMagn. Interference Compat. (INCEMIC)*, 2018, pp. 1–4.
[29] N. Marcuvitz, *Waveguide Handbook*. London, U.K.: IET, 1951.
[30] S. H. Kiani, A. G. Alharbi, S. Khan, M. Marey, H. Mostafa, and M. A. Khan, "Wideband three loop element antenna array for future 5G mmWave devices," *IEEE Access*, vol. 10, pp. 22472–22479, 2022.
[31] G. MacFarlane, "Surface impedance of an infinite parallel-wire grid at oblique angles of incidence," *J. Inst. Electr. Eng.*, vol. 93, no. 10, pp. 1523–1527, 1946.
[32] C.-C. Chen, "Transmission of microwave through perforated flat plates of finite thickness," *IEEE Trans. Microw. Theory Techn.*, vol. 21, no. 1, pp. 1–6, Jan. 1973.
[33] R. Ulrich, K. Renk, and L. Genzel, "Tunable submillimeter interferometers of the Fabry-Perot type," *IEEE Trans. Microw. Theory Techn.*, vol. 11, no. 5, pp. 363–371, Sep. 1963.
[34] S.-W. Lee, G. Zarrillo, and C.-L. Law, "Simple formulas for transmission through periodic metal grids or plates," *IEEE Trans. Antennas Propag.*, vol. 30, no. 5, pp. 904–909, Sep. 1982.
[35] R. Langley and A. Drinkwater, "Improved empirical model for the Jerusalem cross," *IEE Proc. H Microw. Opt. Antennas*, vol. 129, no. 1, pp. 1–6, 1982.
[36] R. J. Langley and E. A. Parker, "Equivalent circuit model for arrays of square loops," *Electron. Lett.*, vol. 18, no. 7, pp. 294–296, 1982.
[37] R. J. Langley and E. A. Parker, "Double-square frequency-selective surfaces and their equivalent circuit," *Electron. Lett.*, vol. 19, no. 17, pp. 675–677, 1983.
[38] C. K. Lee and R. Langley, "Equivalent-circuit models for frequency-selective surfaces at oblique angles of incidence," *IEE Proc. H Microw. Antennas Propag.*, vol. 132, no. 6, pp. 395–399, 1985.
[39] Y. Xu and S. Zhang, "An ultra wideband FSS operating at Ka band," in *Proc. IEEE Int. Conf. Comput. Electromagn. (ICCEM)*, 2019, pp. 1–3.
[40] Y. Ma, W. Wu, Y. Yuan, X. Zhang, and N. Yuan, "A convoluted structure for miniaturized dual-bandstop frequency selective surface," *IEEE Antennas Wireless Propag. Lett.*, vol. 18, no. 2, pp. 328–332, Feb. 2019.
[41] M. I. Hossain, N. Nguyen-Trong, K. H. Sayidmarie, and A. M. Abbosh, "Equivalent circuit design method for wideband nonmagnetic absorbers at low microwave frequencies," *IEEE Trans. Antennas Propag.*, vol. 68, no. 12, pp. 8215–8220, Dec. 2020.
[42] F. Costa, A. Monorchio, and G. Manara, "Efficient analysis of frequency-selective surfaces by a simple equivalent-circuit model," *IEEE Antennas Propag. Mag.*, vol. 54, no. 4, pp. 35–48, Aug. 2012.
[43] D. F. Mamedes and J. Bornemann, "High-gain reconfigurable antenna system using PIN-diode-switched frequency selective surfaces for 3.5 GHz 5G application," in *Proc. SBMO/IEEE MTT-S Int. Microw. Optoelectron. Conf. (IMOC)*, 2021, pp. 1–3.
[44] D. F. Mamedes, A. Gomes Neto, J. C. E. Silva, and J. Bornemann, "Design of reconfigurable frequency-selective surfaces including the PIN diode threshold region," *IET Microw. Antennas Propag.*, vol. 12, no. 9, pp. 1483–1486, 2018.
[45] D. F. Mamedes, J. Bornemann, and A. G. Neto, "Linear-to-circular polarization converter based on four-arms star FSS at 5.2 GHz for 5G applications," in *Proc. 16th Eur. Conf. Antennas Propag. (EuCAP)*, 2022, pp. 1–4.
[46] A. Jabbar, R. Ramzan, O. Siddiqui, M. Amin, and F. A. Tahir, "Wave discrimination at C-band frequencies in microstrip structures inspired by electromagnetically induced transparency," *Sci. Rep.*, vol. 11, no. 1, pp. 1–11, 2021.
[47] L. Zhu, F.-Y. Meng, L. Dong, J.-H. Fu, F. Zhang, and Q. Wu, "Polarization manipulation based on electromagnetically induced transparency-like (EIT-like) effect," *Opt. Exp.*, vol. 21, no. 26, pp. 32099–32110, 2013.
[48] K. Kanjanasit, S. Sanesaowarod, and N. Homsup, "EIT-like effect in metamaterials based on two-layer arrays for high-gain antennas," in *Proc. 17th Int. Conf. Electr. Eng. Electron. Comput. Telecommun. Inf. Technol. (ECTI-CON)*, 2020, pp. 304–307.
[49] M. Rahzaani, G. Dadashzadeh, and M. Khorshidi, "New technique for designing wideband one layer frequency selective surface in X-band with stable angular response," *Microw. Opt. Technol. Lett.*, vol. 60, no. 9, pp. 2133–2139, 2018.
[50] M. C. Neto *et al.*, "Design and synthesis of an ultra wide band FSS for mm-wave application via general regression neural network and multiobjective bat algorithm," *J. Microw. Optoelectron. Electromagn. Appl.*, vol. 18, pp. 530–544, 2019.
[51] C. Jin, Q. Lv, and R. Mittra, "Dual-polarized frequency-selective surface with two transmission zeros based on cascaded ground apertured annular ring resonators," *IEEE Trans. Antennas Propag.*, vol. 66, no. 8, pp. 4077–4085, Aug. 2018.
[52] A. Kesavan, R. Karimian, and T. A. Denidni, "A novel wideband frequency selective surface for millimeter-wave applications," *IEEE Antennas Wireless Propag. Lett.*, vol. 15, pp. 1711–1714, 2016.
[53] A. Chatterjee and S. K. Parui, "A dual layer frequency selective surface reflector for wideband applications," *Radioengineering*, vol. 25, no. 1, pp. 67–72, 2016.
[54] S. Xu *et al.*, "A novel miniaturized ultra-wideband frequency selective surface with rapid band edge," *IEEE Access*, vol. 9, pp. 161854–161861, 2021.

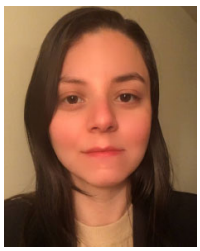

DEISY F. MAMEDES (Member, IEEE) received the B.S. and M.Sc. degrees in electrical engineering from the Federal Institute of Paraiba, Brazil, in 2016 and 2018, respectively. She is currently pursuing the Ph.D. degree in electrical engineering with the University of Victoria, BC, Canada.

She worked as an Instructor with the Federal Institute of Rio Grande do Norte, Brazil, from 2017 to 2018, and with the Senai College of Paraiba, Brazil, from 2018 to 2019. She has authored/coauthored over 35 technical papers. Her research interests include microwave and millimeter-wave components, modeling of integrated circuits, frequency selective surfaces, and antennas.

JENS BORNEMANN (Life Fellow, IEEE) received the Dipl.-Ing. and Dr.-Ing. degrees in electrical engineering from the University of Bremen, Germany, in 1980 and 1984, respectively.

From 1984 to 1985, he worked as an engineering consultant. In 1985, he joined the University of Bremen, Germany, as an Assistant Professor. Since April 1988, he has been with the Department of Electrical and Computer Engineering, University of Victoria, Victoria, BC, Canada, where he became a Professor in 1992. From 1992 to 1995, he was a Fellow with the British Columbia Advanced Systems Institute. In 1996, he was a Visiting Scientist with Spar Aerospace Ltd., (currently MDA Space), Ste-Anne-de-Bellevue, QC, Canada, and a Visiting Professor with the Microwave Department, University of Ulm, Germany. From 1997 to 2002, he was the Co-Director of the Center for Advanced Materials and Related Technology, University of Victoria. In 2003, he was a Visiting Professor with the Laboratory for Electromagnetic Fields and Microwave Electronics, ETH Zurich, Switzerland. From 1999 to 2009, he served on the Technical Program Committee of the IEEE MTT-S International Microwave Symposium. He has coauthored Waveguide Components for Antenna Feed Systems–Theory and Design (Artech House, 1993) and has authored/coauthored more than 350 technical papers. His research activities include RF/wireless/microwave/millimeter-wave components, systems and antenna design, and field-theory-based modeling of integrated circuits, feed networks and antennas. He served as an Associate Editor for the IEEE TRANSACTIONS ON MICROWAVE THEORY AND TECHNIQUES in the area of Microwave Modeling and CAD from 1999 to 2002, and *International Journal of Electronics and Communications* from 2006 to 2008. He is a Registered Professional Engineer in the Province of British Columbia, Canada. He is a Fellow of the Canadian Academy of Engineering and the Engineering Institute of Canada and serves on the editorial advisory board of the *International Journal of Numerical Modelling*.